Chapter-5 Structural and Electrical Properties of Sm-doped..

5.1 Introduction

Donor doped $SrTiO_3$ received much attention due to its high chemical stability, thermal stability, electrical conductivity and tolerance towards carbon or sulfur [36]. It is well known that the oxidation of fuel occurs at triple phase boundary region and mixed (i.e. ionic/electronic) conductivity feature of ceramic based perovskite materials renders the oxide particles as oxidizing reaction sites, which decrease the polarization and accelerate the anode reaction [37]. Anode material is an essential component of solid oxide fuel cells which exhibits high electrical conductivity under reducing condition. $SrTiO_3$ based materials are mainly concerned as anode due to highly active towards the direct oxidation of fuels [37]. The ionic radii of Sm^{3+} (1.24 Å) and Sr^{2+} (1.44 Å) are nearly equivalent which coordinated with O dodecahedrally (AO_{12}). Therefore, Sm^{3+} may be one of the suitable candidates as donor dopant at Sr-site in $SrTiO_3$ and act as anode. It is reported theoretically that Sm-doped $SrTiO_3$ exhibits high thermal expansion coefficient and conductivity [155], [156].

In present chapter, Sm-doped $SrTiO_3$ compositions were synthesized by citrate-nitrate auto-combustion technique and the effect of Sm^{3+} doping on electrical conductivities was studied. The conductivity spectra of the system $Sm_xSr_{1-x}TiO_{3-\delta}$ with x = 0.05, 0.15 and 0.20 at different temperatures have been analysed using Jonscher's power law and conduction mechanism has been explained qualitatively in terms of scaling behaviour. Further, the conductivity was also evaluated from the Nyquist plots and the conduction mechanism was understood in terms of defect chemistry.

5.2 Results and Discussion

5.2.1 Structural Studies

The samples $Sm_xSr_{1-x}TiO_3$ are designated as SST and the compositions with x = 0.05, 0.15 and 0.20 are assigned as SST5, SST15 and SST20, respectively. In $SrTiO_3$, Sr^{2+} (1.44 Å) ion is coordinated with O dodecahedrally (AO_{12}) whereas Ti forms octahedral with O (0.605Å) (BO_6) [112]. According to Goldschmidt relation as given by eq. (1.5), the tolerance factor is found nearly 1, which shows the formation of ideal perovskite structure. Also, the ionic radius of Sm^{3+} in coordination number 12 is 1.24 Å and with the Sm substitution, tolerance factor has been calculated which is observed to decrease from 0.998 to 0.988 with an increase in Sm content as illustrated in fig. 5.1. Hence, Sm^{3+} may be one of the suitable candidates to be substituted at Sr-site as a donor dopant.

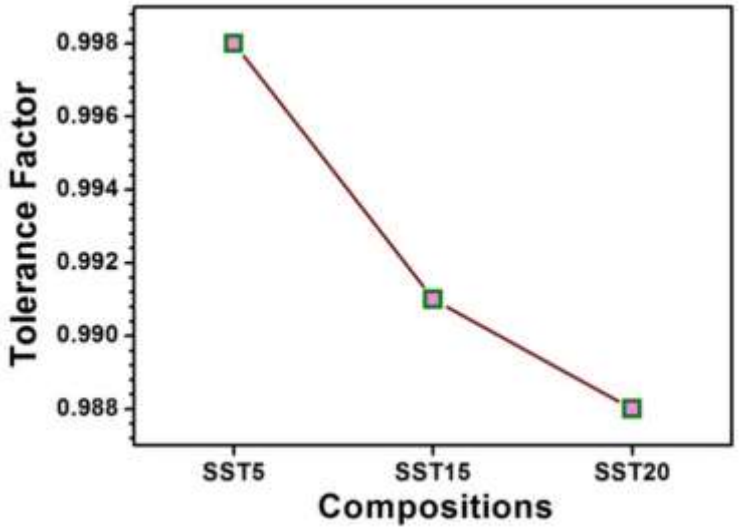

Figure 5.1: The tolerance factor with the compositions.

From XRD patterns, it was found that all the samples show cubic phase with space group $Pm\bar{3}m$ (JCPDS Card Number: 86-0178). No impurity peaks were detected for the samples SST5 and SST15, while for SST20 sample, secondary phase $Sm_2Ti_2O_7$ (JCPDS Card Number: 73-1699) was observed as shown in fig. 5.2 (a). Thus, it is reasonable to

state that the solid solubility limit of Sm in $SrTiO_3$ is less than 20 mol%. On the other hand, the diffraction peaks shift towards higher angle with an increase in the concentration of samarium upto 15 mol% as shown in fig. 5.2 (b). All compositions were refined with Rietveld refinement using FULL PROF Suite software package with Pseudo-Voigt wave function and the results have been observed in fig. 5.2 (a). The background of each profile was approximated by a 6^{th} order polynomial. The lattice parameters, cell volume, some reliability factors of Rietveld refinement are listed in table 5.1 within the porosity and it is clear that the unit cell volume decreases as Sm content increases in $SrTiO_3$ upto 15 mol%, which may be due to the replacement of the larger Sr^{2+} (1.44 Å, CN 12) by the smaller Sm^{3+} (1.24 Å, CN 12) [42], [114] which indicates that the corresponding structural parameters follows Vegard's law [157]–[159].

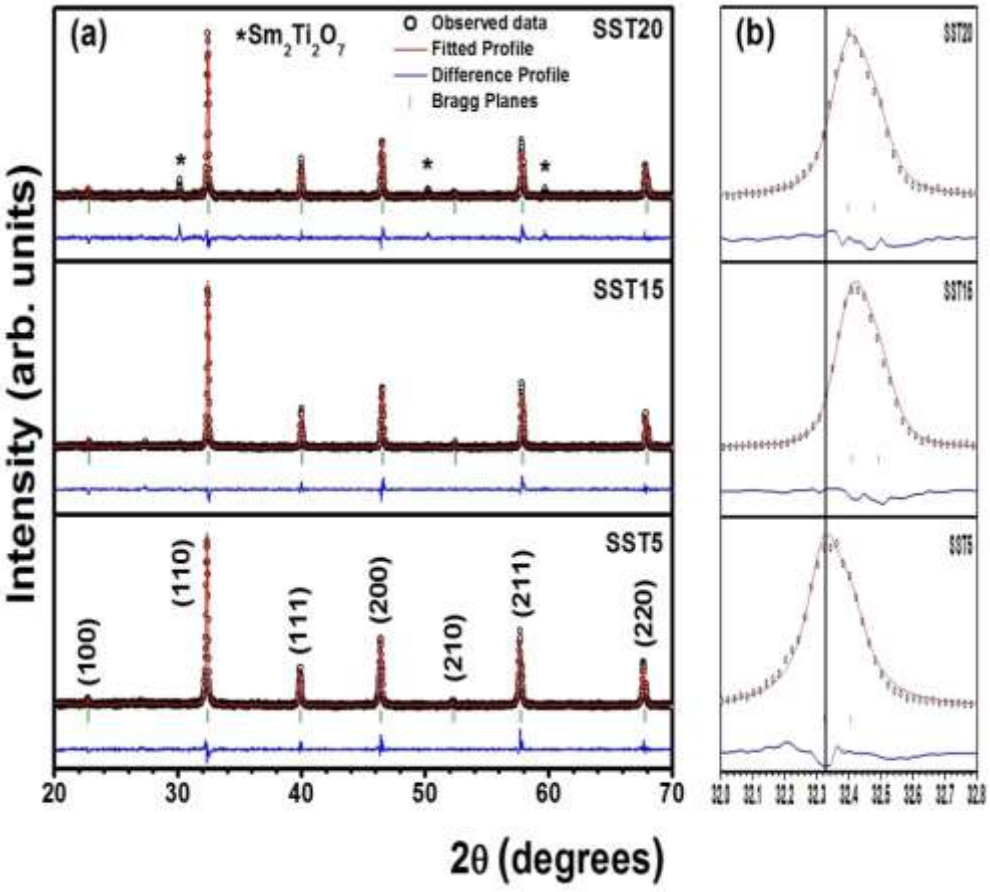

Figure 5.2: (a) The XRD patterns of the sintered samples in air and (b) The shifting of diffraction peaks towards higher angle.

Table 5.1: The lattice parameter, cell volume, Rietveld refined parameters and % porosity of the studied samples.

Sample	Lattice Parameter (Å)	Cell Volume ($Å^3$)	$\chi 2$	Re	R_B	R_F	R_p	R_{wp}	Porosity (%)
SST5	3.9136	59.942	5.14	13.6	5.90	4.13	39.3	32.2	6.3
SST15	3.9031	59.461	5.67	13.6	7.11	5.39	47.5	32.9	40.0
SST20	3.9045	59.525	5.92	15.9	5.86	5.70	59.1	39.4	38.6

Furthermore, fig. 5.3 (a) shows the diffuseness of XRD peak (110) with composition (x) which ensures that the formation of polarons in the system [140], and observed that the diffuseness of XRD peak (110) increases towards left with the increase in Sm mol% in $SrTiO_3$.

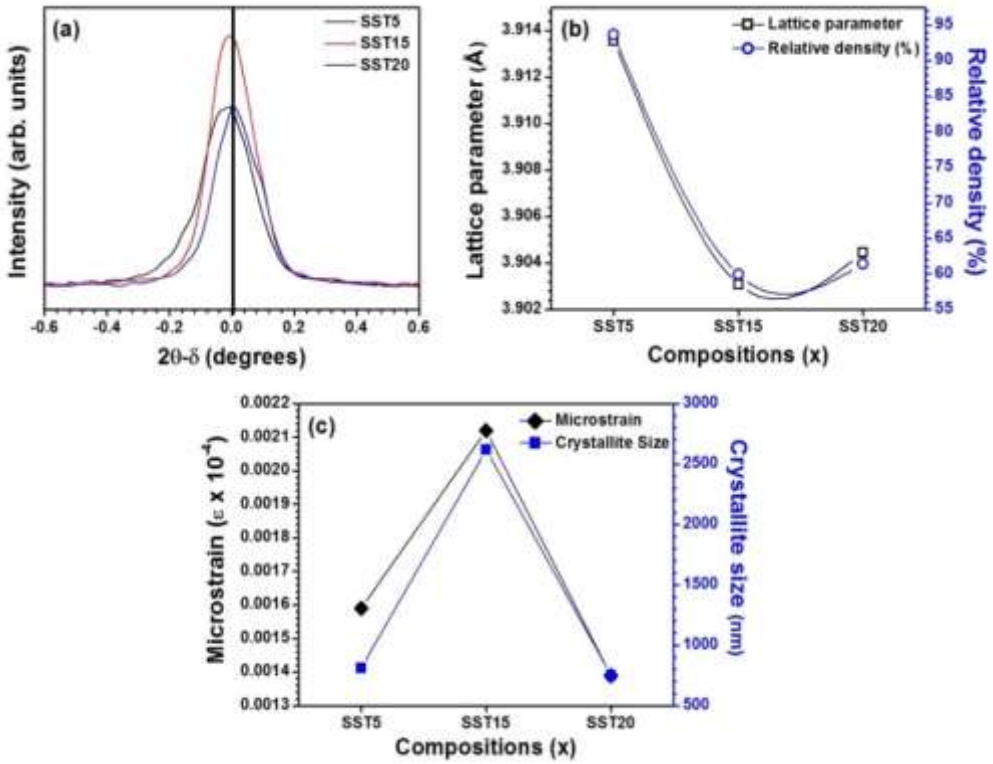

Figure 5.3: (a) Variation of intensity of XRD peak with 2θ-δ (^{o}) where δ is the angle at which maxima occurs showing diffuseness of XRD peak (110) with the compositions, (b) Variation of lattice parameter and relative density with the compositions and (c) Variation of microstrain and crystallite size with the compositions.

Figure 5.3 (b) shows the variation of lattice parameter and relative density with the compositions and depicts that the lattice parameter and relative density follow the same trend which indicates that the lattice parameter and density decrease upto solubility limit

of Sm^{3+}. This can be attributed to the smaller ionic radius of Sm^{3+} in comparison to Sr^{2+}. The microstrain and crystallite size were calculated from XRD patterns by using Williamson-Hall model as given by the eq. (2.1) [82]. Figure 5.3 (c) shows the variation of microstrain and crystallite size with the compositions and observed that the microstrain and crystallite size exhibit the same trend of variation with the compositions i.e. they are increasing with the increase in Sm content upto 15 mol%, while the microstrain and crystallite size decrease for the sample SST20 due to secondary phase formation as shown in fig. 5.2 (a). The microstrain for the sample SST15 was found maximum which may be attributed to a larger amount of defects.

5.2.2 Microstructural Analysis

Figure 5.4 (a)-(c) show the EDAX mapping with FESEM micrographs as shown in the inset. The FESEM micrographs clearly exhibit the grain size evolution are in the order of microns. The average grain sizes of samples were calculated using linear intercept method by ImageJ software and were found to be in the range of 1.8-2.6 μm. The inset FESEM micrographs with grain size histogram plots reveal that the grain size of the sample SST5 is large as compared to the other samples. The relative density of the samples decreases upto 15 mol% and then increases due to the incorporation of secondary phase. Coherently, the porosity of the sample SST15 is found to be 40 % which is highest among the other samples. By increasing the amount of Sm from 5 to 15 mol%, a decrease in the grain size and sinterability is observed as expected for donor doping of $SrTiO_3$ [160]. Excessive Sm-doping with 20 mol% will cause the appearance of secondary phase. Grain growth may become marked with Sm-doping during the sintering process, however, the pyrochlore phase presenting in the sample SST20 may prevent the mass transportation during the sintering process.

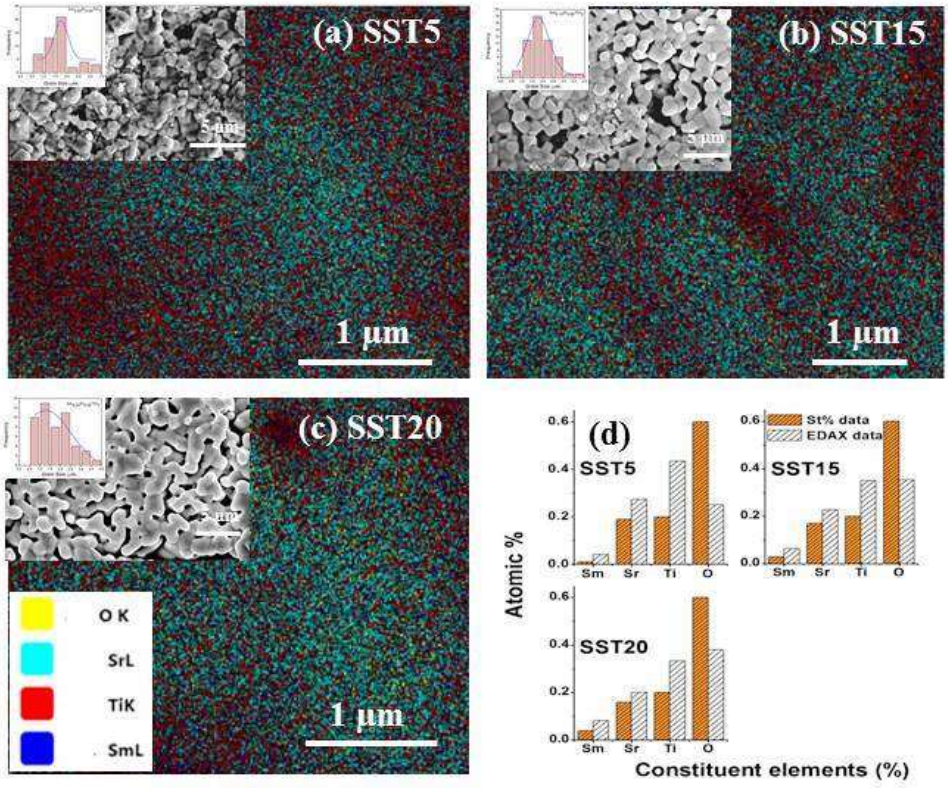

Figure 5.4: The EDAX mapping of the FESEM micrographs as shown in inset of the fractured samples (a) SST5, (b) SST15, (c) SST20 and (d) The stoichiometric and EDAX atomic % for the samples.

The EDAX mapping shows the lesser Oxygen content in the specimens resulting that the samples are oxygen deficient. To analyse further, EDAX data taken from various positions were found to show the elemental composition of all the specimens. Figure 5.4 (d) depicts the stoichiometric and EDAX atomic % for all the compositions. It can be seen that the samples are oxygen deficient and the maximum oxygen deficiency is observed in SST5.

5.2.3 XPS Analysis

EDAX mapping and analysis revealed that the samples are oxygen deficient. To verify the oxygen deficiency in the studied samples, X-ray Photoelectron Spectroscopy (XPS) measurements of each powdered composition were performed. Figure 5.5 (a) shows the oxidation states of the constituent elements in the SST system. The entire XPS spectrum received under the range of 0-1150 eV, consists of core and satellite binding

energy peaks with Sm, Sr, C, Ti and O elements. The binding energy (BE) peaks of the constituent elements are corroborated for different Sm concentration. The presence of a C 1s peak at ~286 eV may originate from external contamination. The binding energies were calculated after calibiration with respect to the C 1s reference peak at ~284.6 eV. The XPS spectra exhibited binding energy peaks of Sm 4d at ~130.8 eV, Sr 3p at ~269.4 eV, Ti 2p at ~459.4 eV, and O 1s at ~530.6 eV as shown in fig. 5.5 (a). With increasing Sm^{3+}doping concentration at Sr-site, the binding energy values shifted to the lower energy side. In the fig. 5.5 (a), a satellite peak of O (KLL) is also detected at ~741.3 eV [152]. Furthermore, O 1s spectral regions are used to detect the existence of oxygen deficiency for the studied compositions.

The O 1s core-level spectra is illustrated in fig. 5.5 (b). The observed peaks for all the compositions in these spectra are broader and asymmetrical in nature.

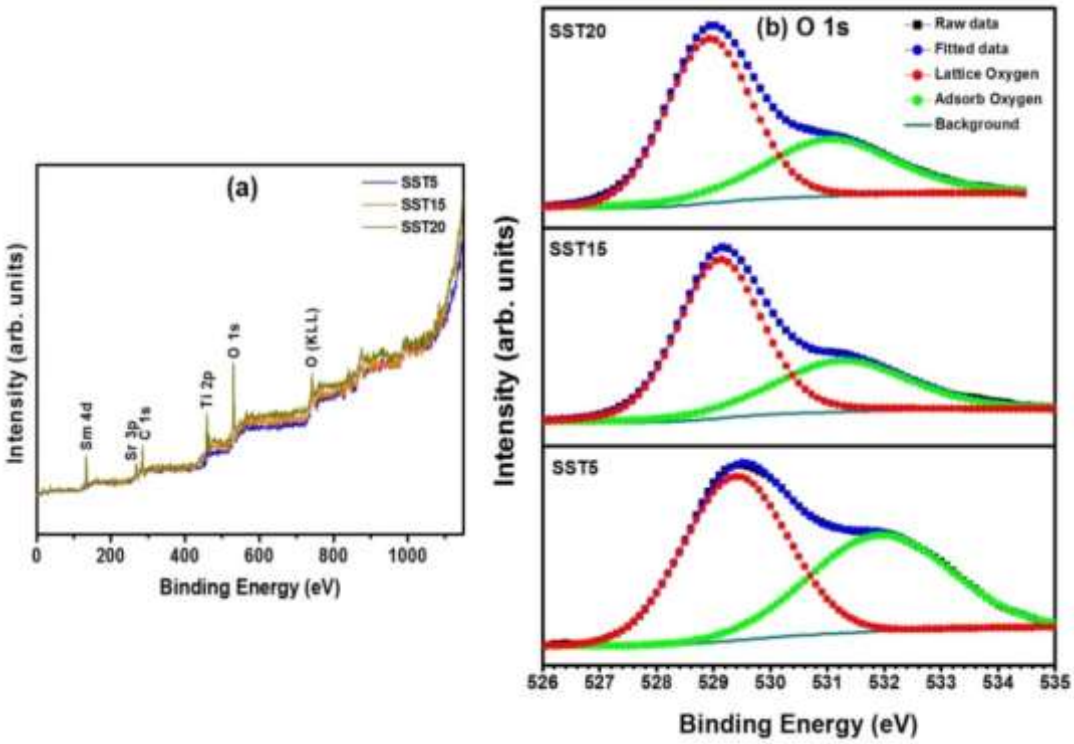

Figure 5.5: (a) The XPS wide spectra of Sm-doped $SrTiO_3$ samples and (b) The illustration of O 1s core level spectra of the samples.

Therefore, the broad peaks might be split into two peaks and assigned as two different oxygen species i.e. lattice and adsorb oxygen [153]. The sample SST15 possess the maximum percentage of lattice oxygen as compared to other samples as illustrated in table 5.2.

5.2.4 Impedance Analysis

The impedance analysis of Sm-doped $SrTiO_3$ samples was performed by using a Frequency Response Analyser (FRA, mod. SALARTRON 1250, Schlumberger) through the four-probe test (Probostat, Norecs) under the frequency range of 1-10^6 Hz. Several models have been suggested to understand the ion dynamics and conduction mechanism. However, in the present system, Jonscher's power law (JPL) has been used to study the ion dynamics of the specimens. The conductivity spectra consist of two components namely dc and ac conductivities. The electrical conductivity can be explained by Jonscher's power law as given by the eq. (2.10) [161].

Figure 5.6 (a) shows the conductivity spectra of the sample SST5 with Jonscher's fitting at measured temperatures. The electrical conductivity under low frequency region is found independent of frequency which corresponds to the dc or bulk conductivity caused by the random motion of charge carriers. However, under high frequency region, successive dispersion occurs representing hopping motion of charge carriers due to relaxation processes and corresponds to ac conductivity [90]. The data points represent by various symbols at measured temperatures have been best fitted. Figure 5.6 (a) clearly indicates that the conductivity spectra of SST5 found to follow Jonscher's Power Law [162]. Also, it was observed that all the other samples also follow JPL at measured temperatures. The variables σ_{dc}, ν_H and n have been obtained by fitting of data points at all the measured temperatures.

The Ghosh scaling of conductivity spectra are scaled with scaling parameters σ_{dc}

and ν_H using the eq. (3.5) [126]. It was observed that the conductivity spectra at measured temperatures do not merge into a single master curve in high frequency range as shown in fig. 5.6 (b). Similar kind of pattern was also observed with Summerfield scaling model in which ν_H introduced as $\sigma_{dc}.T$ as shown in the inset of fig. 5.6 (b). Therefore, all the samples do not follow the time temperature superposition principle in high frequency range. It indicates that the conduction mechanism may be changed along with number of charge carriers with temperature.

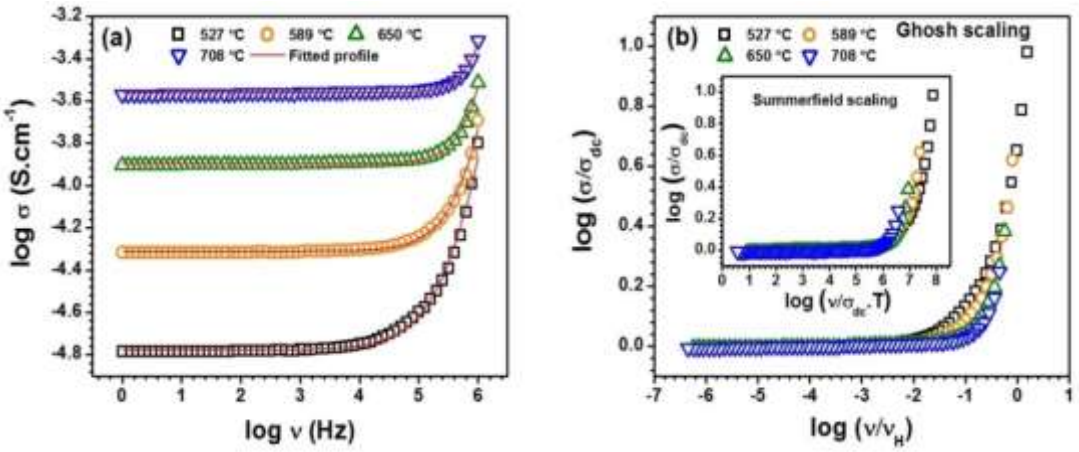

Figure 5.6: (a) The electrical conductivity spectra with JPL fitting and (b) The Ghosh scaling of conductivity spectra with inset of Summerfield scaling at measured temperatures of the sample SST5.

Furthermore, to investigate the electrical conductivity via complex impedance Nyquist plot in which three semi-circular depressed arcs may appear. In general, the arc passing through the origin corresponds to the grains contribution at highest frequency range. While, the second arc corresponds to grain boundaries contribution at the intermediate frequency range and the third arc corresponds to the electrode-specimen interface contribution at the lowest frequency range. The interception of these arcs on the real impedance axis renders the grains, grain boundaries and electrode-specimen interface contribution to the total resistance in the descending order of frequency [163]. Figure 5.7 shows a representative impedance Nyquist plots for SST5 sample at various temperatures in air. It was observed that the sample shows the lowest impedance at a higher

temperature. The complex impedance plane plots for all other studied samples show similar behaviour. In the studied samples, only one semi-circular arc has been observed at measured temperatures due to the grain contribution and the frequency range of these arcs shift to higher frequency side with the increasing temperature. The electrical conductivity of Sm-doped $SrTiO_3$ samples may also be calculated by the eq. (4.3).

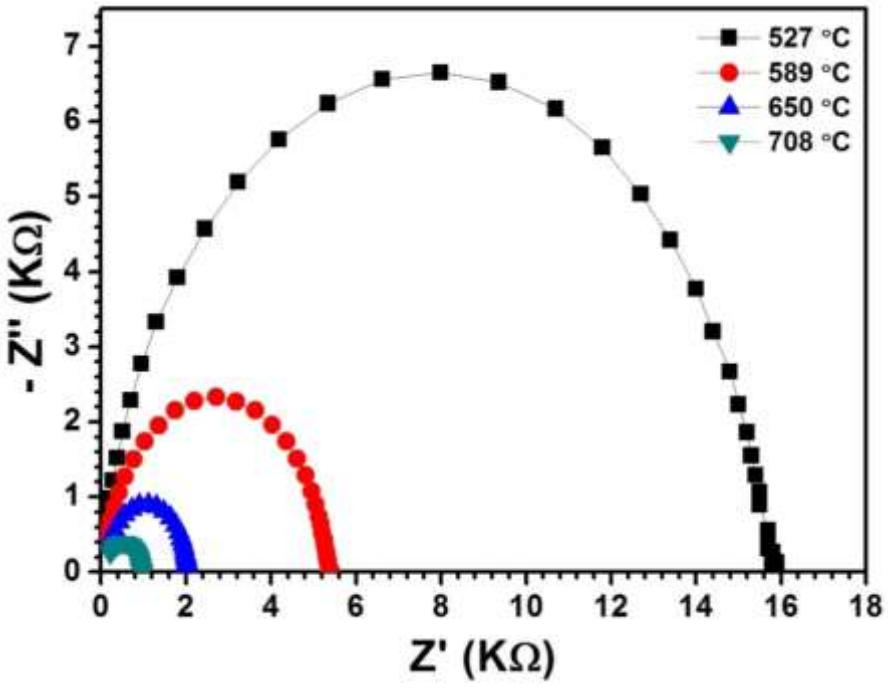

Figure 5.7: The complex impedance Nyquist plots of the sample SST5 at measured temperatures.

The electrical conductivity of all compositions has been calculated by Jonscher's power law in air and hydrogen atmosphere. Thereafter, the activation energy of conduction for all studied compositions was calculated by using the Arrhenius eq. (4.4) [164].

The Arrhenius plots of log (σT) *vs.* 1000/T for Sm-doped compositions in H_2 atmosphere is shown in fig. 5.8 (a). The Arrhenius plot exhibits two slopes in the two temperature ranges (i.e. 200-400 ºC, 400-700 ºC) for the studied samples [40] as shown in fig. 5.8 (a) and (b). The maximum activation energy (Ea) is found to be 0.325 eV for the system in H_2 atmosphere which indicates high electronic contribution as reported in table

5.2. It was observed that SST20 possesses the highest conductivity (i.e. 1.4×10^{-1} S.cm^{-1} at 675 ^{o}C) with lowest activation energy.

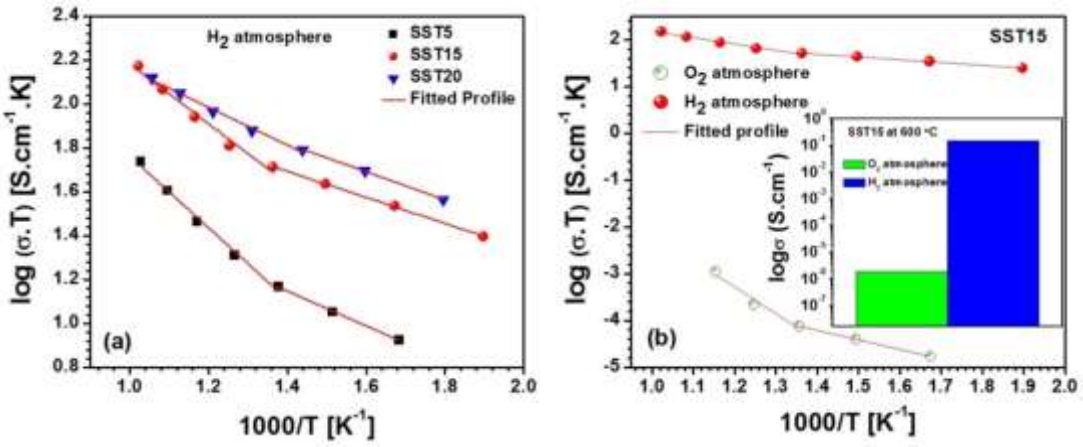

Figure 5.8: (a) The Arrhenius plot (log σT vs. 1000/T) for the all studied samples and (b) The comparative Arrhenius plot with inset conductivity plot at 600 ºC for the sample SST15 in O_2 and H_2 atmospheres.

Table 5.2: Activation energy and lattice oxygen content of all the studied samples.

Sample	E_a (eV) H_2 atmosphere		Lattice oxygen (%)
	200-400 ºC	400-700 ºC	
SST5	0.135	0.325	20.94
SST15	0.118	0.271	45.34
SST20	0.127	0.172	39.87

The comparative Arrhenius plot with inset conductivity plot at 600 ºC for the sample SST15 under both atmosphere is shown in fig. 5.8 (b). It was observed that SST15 is also possessing higher conductivity (i.e. 1.5×10^{-1} S.cm^{-1} at 700 ^{o}C) in H_2 atmosphere. The activation energy lower than 0.5 eV, indicates that the samples contribute to more electronic conductivity rather than ionic conductivity [165].

The lattice oxygen may be lost under reducing atmosphere and thus oxygen vacancies will be generated as per the eq. (1.19). In order to conserve the electro-neutrality, the following equation must be satisfied.

$$[Ti'_{Ti}] = [Sm^{\bullet}_{Sr}] + 2[V_O^{\bullet\bullet}] \qquad (5.1)$$

Therefore, both extrinsic defects introduced by Sm incorporation at Sr-site and intrinsic oxygen vacancies, which are formed under reducing conditions, contribute to the formation of electrons and increase of conductivity [78].

5.2.5 Chemical Stability

The investigation of chemical stability for the reduced samples was performed by XRD measurements and FESEM micrographs. From the results as reported in fig. 5.9, it was observed that the XRD patterns of the samples SST5, SST15 and SST20 show no signs of chemical and structural degradations. In addition, corresponding FESEM micrographs of reduced samples (inset in fig. 5.9) also confirm that all the samples are chemically stable. Moreover, for all the samples, the peaks have been shifted towards the right as shown in the inset of fig. 5.9 for SST5 in the reducing atmosphere showing lattice contraction. The lattice contraction may be attributed to increasing the defects along with oxygen vacancies under reducing atmosphere [166].

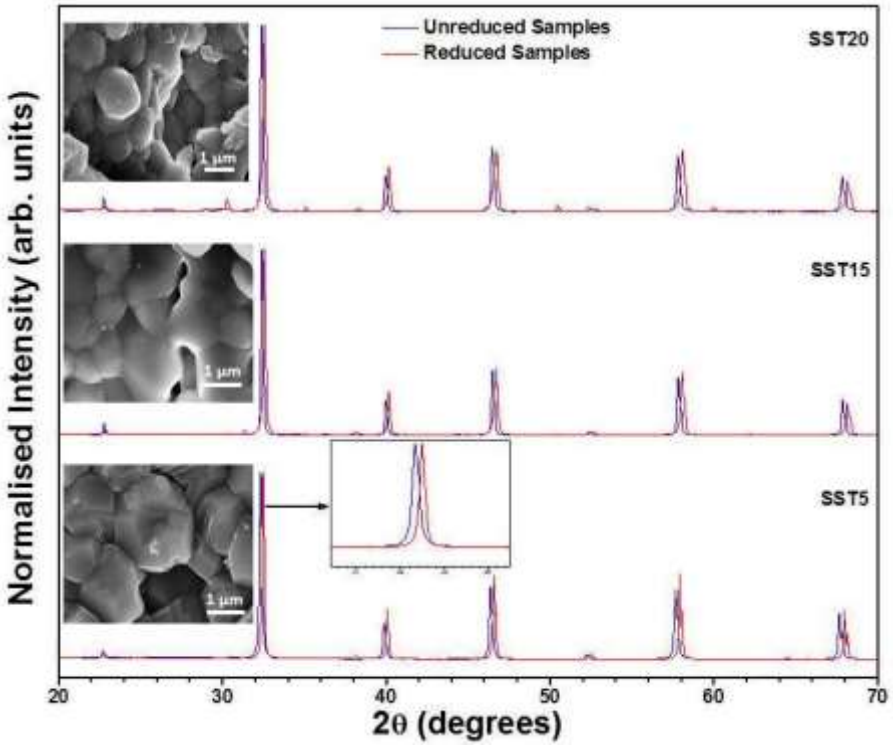

Figure 5.9: XRD patterns of unreduced and reduced samples and inset FESEM micrographs of reduced samples.

Amongst all the investigated samples, the most promising anodic material for SOFCs is $Sm_{0.15}Sr_{0.85}TiO_3$ due to its excellent chemical stability without involvement of secondary phase coupled with high conductivity and low activation energy under reducing condition.

5.3 Conclusions

In this chapter, Sm-doped $SrTiO_3$ are considered to be studied and its structural and electrical properties were investigated to check its suitability as anode, which exhibit high electrical conductivity with excellent chemical stability in hydrogen atmosphere. It is observed that with the increase in Sm substitution, simultaneous incorporation of Sm at Sr- and Ti-sites or incorporation of Sm at Sr-site along with electron compensation take place. Therefore, there is a decrease in lattice parameters upto solubility limit. The sample SST15 shows higher electronic conductivity rather than ionic conductivity without involvement of secondary phase. Hence, the sample SST15 may be considered as a suitable anode material for SOFCs.